12^{th} International Conference on Fracture Mechanics of Concrete and Concrete Structures
FraMCoS-12
B.L.A. Pichler, Ch. Hellmich, P. Preinstorfer (Eds)

https://doi.org/10.21012/FC12.1358
MS13-2:1

MULTIPHYSICS MODELLING FOR 3D CONCRETE PRINTING: FROM PRINTABILITY TO HARDENED PROPERTIES

M. PIERRE*, **S. GHABEZLOO***, **P. DANGLA***, **R. MESNIL***, **M. VANDAMME*** **AND J.-F. CARON***

* Navier, ENPC, Institut Polytechnique de Paris, Univ Gustave Eiffel, CNRS
6-8 Avenue Blaise Pascal, 77455 Marne-la-Vallée Cedex 2, France
e-mail: maxime.pierre@enpc.fr

Key words: Poromechanics, 3D Concrete Printing, Numerical Modelling

Abstract. 3D-printing with cement-based materials has gained attractiveness in recent years thanks to freedom of form allowing for mass customization, as well as reduced material consumption through shape optimization. However, reaching repeatable quality standards and predictable mechanical properties for print pieces remains a challenge which modelling could help solving. We thus propose a simulation framework for 3D-printing of cement-based materials with two main components. Firstly, we present a fully coupled thermo-hydro-mechanical constitutive model, extended from classical poromechanics to chemically solidifying media, wherein material properties evolve with the extent of hydration reactions, allowing to cover behaviours from the very-early age to the hardened state, along with some experimental procedures to determine model parameters. Secondly, a finite element-based modelling strategy is introduced, aimed at creating a digital twin of the printing process, namely the sequential deposition of the material throughout the print path. Such a framework allows the investigation of common issues in 3D-printing of cement-based materials along with their multi-physics origins, ranging from printing failures to longer-term durability concerns. Influence of process-related parameters -such as layer-pressing- and environmental conditions on printing stability and accuracy are displayed, along with indication as to their mitigation. Durability issues related to drying, be it at the interlayer or at the exterior surface of a print piece, are also presented in light of a detailed modelling of unsaturated behaviour from the constitutive model.

1 INTRODUCTION

3D concrete printing has emerged in the past few years as a new technology with the potential to profoundly disrupt the construction sector by proposing some answers to long-standing issues. The construction industry is facing what can be qualified as a productivity crisis, with a productivity that has hardly improved if not regressed over the past decades, and lagged significantly behind other manufacturing sectors. Bringing construction to the era of automation, otherwise known as “industry 3.0” could help bridge part of the productivity gap with the rest of the industry, which is one of the promises of 3D printing. In addition, environmental concerns with the realization that a drastic reduction of global greenhouse gas emissions is necessary in the coming years in order to limit the consequences of climate change also beg for a reduction in material consumption. Cement-based materials, in particular, are deemed to be responsible of around 8% of the global CO_2 emissions through their production, so that a strong decrease in production volumes is mandatory in future years. By allowing operators to deposite material precisely where it is needed, 3D printing technologies allow to optimize the quantity of material used and thus reduce material consumption when compared with equivalently functional cast concrete pieces. However, a number scientific challenges are yet to be overcome before 3D concrete printing can be widely adopted throughout the industry. Herein, we will look into two specific issues.

A first issue resides in the prediction of "buildability", that is to say foresee whether a certain geometry, given certain process parameters and environmental conditions, can be successfully printed without it collapsing. This requires a very fine knowledge of cement-based materials at the very-early age, as the fluid-to-solid transition has just begun. Especially in printing technologies using accelerating admixtures, such as aluminium sulphate, to obtain a rapidly setting mortar, the material evolves quickly, at the same time as stresses inside the structure increase due to the sequential deposition of the different material layers. A second issue regards the hardened properties of the printed material. Beyond providing mechanical support until the material is hardened, the formwork used in concrete casting is also a formidable shield to prevent moisture evaporation. 3D printed pieces are on the contrary directly subjected to evaporation, a phenomenon all the more detrimental in this case due to the slender nature of typical 3D printed structures. With higher surface to volume ratios, printed pieces dry quickly, which has a negative impact on hydration which stops prematurely due to the lack of free water availability in the material. This results in lower mechanical performances when compared with identical cast material [5].

Phenomena at work when tackling these issues are by nature coupled between several physics: chemo-mechanical hardening determines whether a material evolves fast enough to support its self-weight, while hydro-chemical couplings and transport in the pore network of the material are at the heart of strength loss due to curing conditions. To address these different issues in a unified way, we propose to use a chemo-thermo-poromechanical model adapted to 3D printing mortars. After a short introduction of the model components, we will first show how a specially developed code based on the finite element method (FEM) can reproduce the printing process, and in particular the sequential deposition of the material, in order to provide buildability predictions. Results are shown on a sample geometry considering a range of process parameters. Then, we are interested in determining the hardened properties of the printed piece, depending on the curing conditions (temperature and relative humidity). To this end, we devise a simple evaporation experiment, and comparison between experimental results and simulation outputs provides validation of the model and boundary conditions. Finally, the impact of the drying process on the material porperties are shown, correlating with the strength loss which is experimentally observed.

2 MODEL BACKGROUND

2.1 Constitutive relationships

The constitutive model used herein derives from that proposed with application to class G cement paste by Pierre et al. [1]. We quicly recall here the main ingredients of this chemo-thermo-poromechanical model. The state equations for the solid skeleton read:

$$\begin{aligned}
\mathrm{d}\underline{\underline{\sigma}}\big|_{S_l} &= \mathbb{C}(\xi) : \mathrm{d}\underline{\underline{\varepsilon}}^{el} - b(\xi) S_l \mathrm{d}p_l - 3\kappa(\xi)\mathrm{d}T, \\
\mathrm{d}\varphi\big|_{S_l} &= b(\xi)\,\mathrm{tr}(\mathrm{d}\underline{\underline{\varepsilon}}^{el}) + \frac{\mathrm{d}p_l}{N(\xi)} - 3\alpha_\varphi(\xi)\mathrm{d}T, \\
\mathrm{d}S_s\big|_{S_l} &= 3\kappa(\xi)\,\mathrm{tr}(\mathrm{d}\underline{\underline{\varepsilon}}^{el}) - 3\alpha_\varphi S_l \mathrm{d}p_l \\
&+ (1-\phi_0(\xi))\frac{C_{\sigma_s}}{T}\mathrm{d}T, \qquad (1)
\end{aligned}$$

where $\underline{\underline{\sigma}}$ is the Cauchy stress tensor, $\mathbb{C}$ fourth order stiffness tensor, ξ is the extent of the hydration reaction, $\underline{\underline{\varepsilon}}^{el}$ is the elastic part of the linearized strain tensor, b is Biot's coefficient, S_l is the liquid saturation degree, p_l is the liquid pore pressure, $\kappa = \alpha_s K$ where α_s is the solid's heat expansion and K the skeleton's bulk modulus, T is the temperature, φ is the porosity variation due to mechanical actions (not accounting for variations due to that of the solid fraction), N is Biot's modulus, $\alpha_\varphi = \alpha_s(b(\xi) - \phi_0(\xi))$ is the thermal expansion of the pores, S_s is the entropy of the solid phase and C_{σ_s} is the solid's volumetric heat capacity at constant stress. The so-called "initial porosity" ϕ_0 varies with hydration as solid hydrates are newly formed:

$$\mathrm{d}\phi_0 = -\Delta\overline{V}_s \mathrm{d}\xi, \tag{2}$$

where $\Delta\overline{V}_s$ is the molar volume change of solid in the hydration reaction.

In addition, two types of inelastic strains are considered: plastic strains and chemical expansion strains. Plastic strains evolve according to a Cam-Clay-type yield surface of equation:

$$\begin{aligned} f(\sigma',\tau) &= \tau^2 \exp\left(k\frac{2\sigma' + \sigma_t - \sigma_c}{\sigma_t + \sigma_c}\right) \\ &+ M^2(\sigma' - \sigma_c)(\sigma' + \sigma_t), \end{aligned} \tag{3}$$

where $\sigma' = \mathrm{tr}(\underline{\underline{\sigma}})/3 + p_l$ is the mean effective stress,τ the von Mises norm of the deviatoric stress, σ_c and $\sigma_t = f_t\sigma_c$ are the isotropic limits in compression and tension, respectively, M is the friction ratio and k a material parameter. This yield surface is coupled with the following chemo-mechanical hardening laws [1]:

$$\begin{aligned} \mathrm{d}\sigma_c &= h_\varepsilon \sigma_c \mathrm{d}\varepsilon^p_V + h_\xi \Delta\overline{V}_s \mathrm{d}\xi, \\ \mathrm{d}M &= M_\xi \Delta\overline{V}_s \mathrm{d}\xi, \end{aligned} \tag{4}$$

so that the yield surface evolves with hydration as shown in Figure 1.

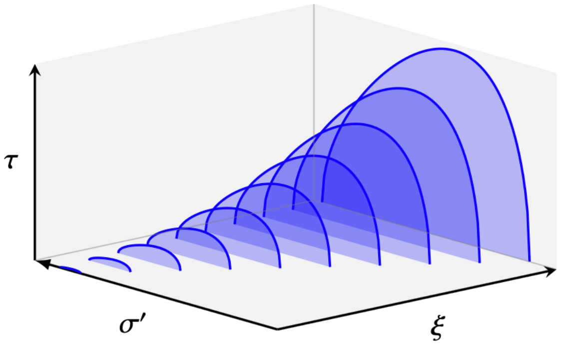

Figure 1: Yield surface evolution with hydration.

Strains due to chemical expansion (for instance, in the case of production of ettringite from the addition of $\mathrm{Al_2(SO_4)_3}$-based accelerators), are supposed isotropic and linearly related to the hydration extent ξ:

$$\mathrm{d}\varepsilon^{exp} = \varepsilon_\xi \mathrm{d}\xi. \tag{5}$$

The liquid saturation degree S_l is related to the capillary pressure p_c through a van Genuchten-type equation [7] integrating a dependence to the hydration extent ξ:

$$\begin{aligned} S_l(p_c,\xi) &= \left(1 + \left(\frac{p_c}{p_r(\xi)}\right)^n\right)^{\frac{1-n}{n}}, \\ p_r(\xi) &= p_{r,0} \exp\left(k_{sl}\xi\right), \end{aligned} \tag{6}$$

where n, $p_{r,0}$ and k_{sl} are material parameters.

The hydration extent ξ evolves with the following kinetics [4]:

$$\begin{aligned} \dot{\xi} &= \beta_{RH}\frac{k_\xi}{\eta(\xi)}\left(\frac{\mathcal{A}_0}{k_\xi \xi_\infty} + \xi\right)(\xi_\infty - \xi) \\ &\times \exp\left(-\frac{E_A}{RT}\right), \\ \eta(\xi) &= \eta_0 \exp\left(-\bar{\eta}\frac{\xi}{\xi_\infty}\right), \end{aligned} \tag{7}$$

where β_{RH} represents the slow-down of the reaction at lower relative humidity [2], k_ξ, $\mathcal{A}_0$, η_0 and $\bar{\eta}$ are material parameters, ξ_∞ is the ultimate hydration extent, and E_A is the activation energy.

2.2 Balance equations

In addition to the material behaviour at the integration point, we consider the following balance equations. For the momentum balance:

$$\underline{\nabla} \cdot \underline{\underline{\sigma}} + \rho\underline{\gamma} = 0, \tag{8}$$

where ρ is the materials density and $\underline{\gamma}$ gravity's acceleration.

The water mass balance equation takes into account the sink term from water consumption by the chemical process, as follows:

$$\dot{m}_w = \underline{\nabla} \cdot \underline{M}_w + \nu_w \mathcal{M}_w \dot{\xi}, \tag{9}$$

where m_w is the fluid mass per unit material volume, $\underline{M}_w$ is the fluid mass flux vector, ν_w represents the stoichiometry of water in the hydration reaction, and $\mathcal{M}_w$ is water's molar mass. The fluid mass vector is expressed by Darcy's law:

$$\underline{M}_w = k_l(S_l, \phi)\frac{\rho_w}{\eta_w}\underline{\nabla p_l}, \tag{10}$$

where ρ_w and η_w are the density and viscosity of water, respectively, and the liquid permeability k_l depends on the saturation degree (Mualem's model [8]) and porosity (Taylor's model):

$$\begin{aligned} \left.\frac{k_l(S_l)}{k_l(1)}\right|_e &= \sqrt{S_l}\left(1-\left(1-S_l^{\frac{n}{n-1}}\right)^{\frac{n-1}{n}}\right)^2, \\ \left.\frac{\partial k_l}{\partial \phi}\right|_{S_l} &= \frac{k_l \ln(10)}{C_{kl}(1-\phi)^2}, \end{aligned} \tag{11}$$

where C_{kl} is a material parameter.

The entropy balance equation includes the latent heat of hydration, so that it reads:

$$T\left(\dot{S} - \underline{\nabla}\cdot\left(s_w\underline{M}_w\right)\right) = -\underline{\nabla}\cdot\underline{q} + L\dot{\xi}, \tag{12}$$

where S is the total entropy (solid + fluid), s_w is water's specific entropy, $\underline{q}$ is the heat flux and L the latent heat of hydration. The heat flux is obtained by means of Fourier's law:

$$\underline{q} = -k_T\underline{\nabla T}, \tag{13}$$

where k_T is the thermal conductivity.

3 MATERIALS AND METHODS

3.1 Mortar mix

The considered material is a 3D printing mortar used at Navier Lab, based on a pre-mix from Holcim (NAG3). The mass proportions of pre-mix, water and additives is given in Table 1 for 1 kg of material prior to the introduction of the accelerator. The mortar was mixed for 5 minutes before adding the accelerator, then mixed one more minute.

Table 1: Mix proportions for the used mortar

Material	Quantity
Premix	908 g
Water	88 g
Superplasticizer	4 g
Accelerator	6 g

3.2 Evaporation experiment

A simple evaporation experiment is devised in order to validate the model in this setting. As seen in Figure 2, a parallelepipedic slab of the abovementionned mortar is cast and subsequently placed on a scale, while its surface temperature is monitored by means of a thermocouple. The measured weight evolution gives access to the evaporated water mass.

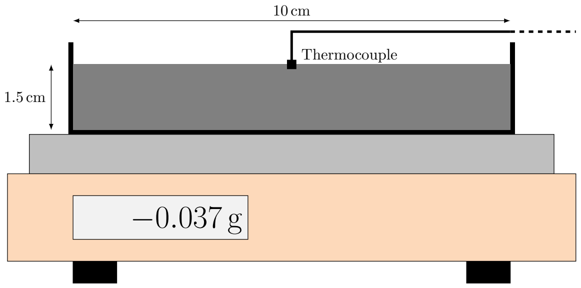

Figure 2: Yield surface evolution with hydration.

The sample is left to dry for a week at a room temperature around 22 °C and a relative humidity close to 50%.

4 PARAMETER DETERMINATION

Parameters of the material model are determined as much as possible from independent experiments. Hydration kinetics laws are fitted using data from P-wave velocities during hydration. The specificity of accelerated mortars such as the one used here, is its hydration kinetics which can be decomposed in two main phases. As seen in Figure 3, a first significant increase of the P-wave velocity is observed in the first hour following the introduction of the accelerator, which corresponds to the early precipitation of ettringite. In a second time, what we will refer to as "main binder hydration" occurs, and is akin to the usually expected hydration kinetics of an unaccelerated mortar. In face of the different natures and time scales of these two hydration events, it is convenient to separate them into two distinct processes with associated hydration extents ξ_1 and ξ_2, as illustrated in Figure 3. This allows to perfectly describe the entirety of the complex hydration process of our accelerated mortar.

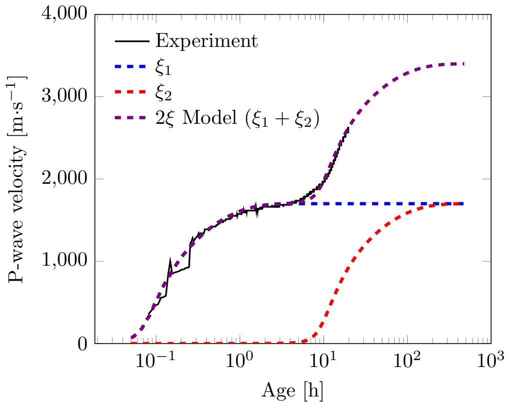

Figure 3: Accelerated mortar kinetics fitting as the sum of two reaction extents (ξ_1, ξ_2).

Parameters of the water retention curve are determined using freeze-drying of the sample at given hydration degrees followed by mercury intrusion porosimetry. Stiffness and strength evolution parameters were calculated from uniaxial tests at different times. Other parameters were taken from literature, or, in the case of the initial permeability at early age, fitted to experiments. Table 2 gives a comprehensive overview of parameters. Parameters linked with the hydration process have been doubled, with

5 PRINTING PROCESS SIMULATION

5.1 Finite element strategy

An accurate representation of the printing process in simulation requires a strategy to handle the sequential deposition of the material. A simulation framework was developped using `FEniCS` [6] aimed at the simulation of the printing process. In addition to the material model presented above, it handles the sequential deposition of the material by adding a slice of the mesh after each calculation time step. The mesh is constructed automatically from the printpath data of the robot, which holds the information of the robot's consecutive positions. This mesh is segmented into printing layers, and each layer in smaller sections, which can be added sequentially. At each time step's beginning, the results from the previous time step are used as initial values in the part of the mesh that already existed at the previous time step, while default initial values are used in the newly added mesh segment.

Table 2: Model parameters

$E(\xi = 0)$	0.1 MPa
$E_{\xi,1}$	17 GPa
$E_{\xi,2}$	400 GPa
ν	0.2
K_s	135 GPa
α_s	$1 \cdot 10^{-5}$ K^{-1}
$C_{\sigma s}$	$2.4 \cdot 10^{6}$ J·K^{-1}·m^{-3}
L_1	$4.52 \cdot 10^{5}$ J·mol^{-1}
L_2	$1.04 \cdot 10^{5}$ J·mol^{-1}
$\phi_0(0)$	0.198
$\Delta\overline{V}_{s,1}$	$5.74 \cdot 10^{-4}$ m^3·mol^{-1}
$\Delta\overline{V}_{s,2}$	$9.36 \cdot 10^{-5}$ m^3·mol^{-1}
ε_V^{ξ}	$1.8 \cdot 10^{-3}$ m^3·mol^{-1}
$\xi_{1,\infty}$	20 mol·m^{-3}
$\xi_{2,\infty}$	1000 mol·m^{-3}
$E_{A,1}$	$4.155 \cdot 10^{4}$ J·mol^{-1}
$E_{A,2}$	$3.458 \cdot 10^{4}$ J·mol^{-1}
ΔV	$1.84 \cdot 10^{-5}$ m^3·mol^{-1}
$\mathcal{A}_{0,1}/k_{\xi,1}$	8609 mol^2·m^{-6}
$k_{\xi,1}/\eta^0_{\xi,1}$	18.46 m^3·mol^{-1}·s^{-1}
$\overline{\eta}_1$	2.96
$\mathcal{A}_{0,2}/k_{\xi,2}$	0.14 mol^2·m^{-6}
$k_{\xi,2}/\eta^0_{\xi,2}$	8000 m^3·mol^{-1}·s^{-1}
$\overline{\eta}_2$	2.0
$\nu_{w,1}$	32
$\nu_{w,2}$	6
p_r	0.6 MPa
n	2.7
$k_{sl,1}$	0
$k_{sl,2}$	4
k	-0.7
$h_{\xi,1}$	80 MPa
$h_{\xi,2}$	2000 MPa
h_{ε}	80
$M(\xi = 0)$	0.4
$M_{\xi,1}$	35
$M_{\xi,2}$	7
f_t	0.1
k_T	1.5 W·m^{-1}·K^{-1}
$k_l(e_0)$	$4 \cdot 10^{-18}$ m^2
C_{k_l}	3

This way, the material evolves seemlessly in time, and the age of the material depends on the time at which it was deposited, as occurs in reality. Figure 4 depicts this numerical deposition process in a 3D setting.

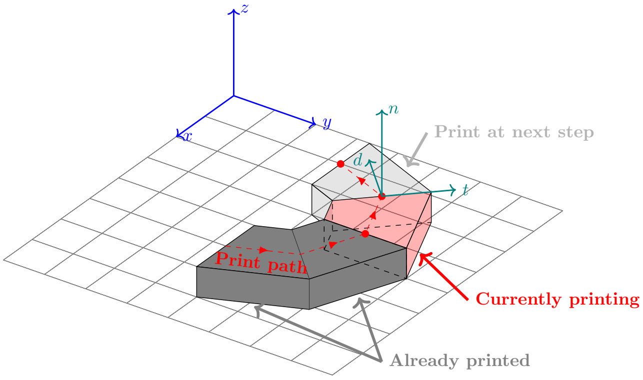

Figure 4: Simulation strategy to model material deposition. Mesh segments are added sequentially along the printpath.

5.2 An example simulation

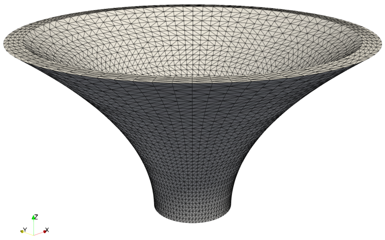

Figure 5: Meshed geometry of the object of interest.

We propose to simulate the printing process of a vase-like shape presented in Figure 5. A printing speed of $10\,\mathrm{cm{\cdot}s^{-1}}$ is first considered. Experimentally, this shape was observed to failed in a peculiar way: namely, the bottom layers would remain intact while the top part of the structure would fall over to the sides, as can be seen in Figure 6.

Figure 6: Experimentally-observed failure mode of the studied geometry.

On the simulation side, we look at the time and location of the onset of plastic strains. Figure 7 shows a $x - z$ cut of the object with values of the equivalent plastic strain, upon first appearance of plastic strains. It can be observed indeed that plastic strains originate not from the bottom layer as is generally assumed, but rather from an intermediate layer. In fact, plasticity does not propagate downward in this case, which is consistent with the experimentally-observed failure mode. The model is in this case capable of explaining the failure mechanism, which stems from a subtile competition between the rate of evolution of strength from the hydration reaction and the rate of increase of stresses from layer stacking.

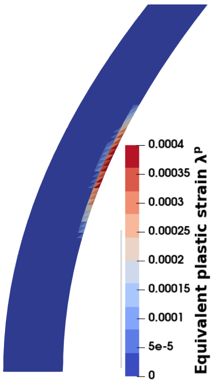

Figure 7: Simulated location of plasticity onset in an $x - z$ slice of the object.

5.3 Printing parameters influence

Numerous printing parameters and environmental parameters such as temperature have an influence on the printing process. Herein, we elect to look at two parameters: printing speed and ambient temperature. The former is obviously determinent in the printability of a particular object, as there is a speed limit above which the object is not going to be printable anymore. The latter is also of importance, mainly due to the temperature dependence of the hydration kinetics, as highlighted in Equation (7). Elevated temperatures are thus in theory beneficial from the viewpoint of printability. Figure 8 shows a heatmap of the maximum number of printable layers as a function of both printing speed and temperature, considering the previous geometry. Intuitively, the number of printable layers decrease with increasing printing speed and increase with increasing temperature. Such an analysis is interesting, because it can help plan a different printing speed ahead of time if the printing environment was changed from one printing session to another. The graph in Figure 8 can serve as a basis to modulate the printing speed in case of a temperature change, in order to retrieve similar printing conditions.

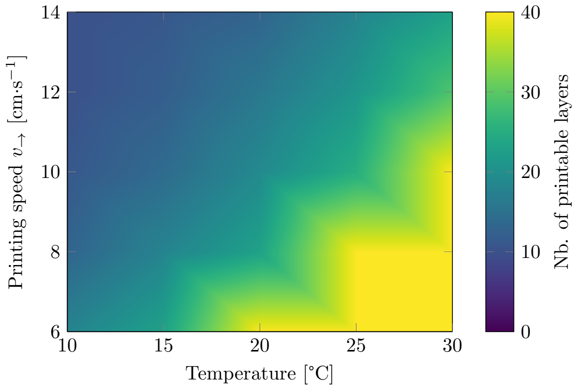

Figure 8: Maximum number of printable layers as a function of printing speed and room temperature.

6 EVAPORATION AND HARDENED PROPERTIES

Successfully printing the desired object is not the only challenge in 3D concrete printing. Determination of the object's hardened properties is also not straightforward, as they are significantly influenced by curing conditions. In this section, we will show that the presented model with adequate boundary conditions is coherent with evaporation experiments and is able to explain the observed strength loss.

6.1 Boundary conditions

In order to simulate evaporation processes, we need a set of suitable boundary conditions, in both fluid and heat fluxes. The evaporation rate at the surface of concrete is usually taken proportional to the difference of water vapour pressure between the material and the environment [3]:

$$W = A(p_{sat}(T)R_{H,int} - p_{sat}(T_{ext})R_{H,ext}), \quad (14)$$

where $A = 2.19 \cdot 10^{-8}\,\mathrm{s{\cdot}m^{-1}}$ is a proportionality coefficient usually deemed dependent on the wind speed, which is considered null here. Heat exchanges at the evaporation surface are considered to be of two natures. First, there is a heat transfer due to water's vaporisation enthalpy $\Delta H_{vap} = 44.2\,\mathrm{kJ{\cdot}mol^{-1}}$:

$$Q_{evap} = \frac{\Delta H_{vap}}{\mathcal{M}_w} W. \quad (15)$$

In addition, we consider heat convection in the form:

$$Q_{conv} = h_{conv}(T - T_{ext}), \quad (16)$$

where h_{conv} is the heat transfer coefficient with air taken as $25\,\mathrm{W{\cdot}K^{-1}{\cdot}m^{-2}}$. All three boundary conditions are applied at the evaporation surface in an FEM calculation which mimics the evaporation experiment presented in Section 3.

6.2 Experimental and simulation results

Figure 9 shows the evolutions of the mass and surface temperature of the hydrating mortar for the first 15 days after casting. It can be seen that most of the evolution occurs in the first two days, with mass slowly stabilising and temperature oscillating around 22 °C due to variations in room temperature. Initially, the surface temperature of the mortar is far above room temperature, as high as 29 °C, which quickly drops to below room temperature in the first few hours.

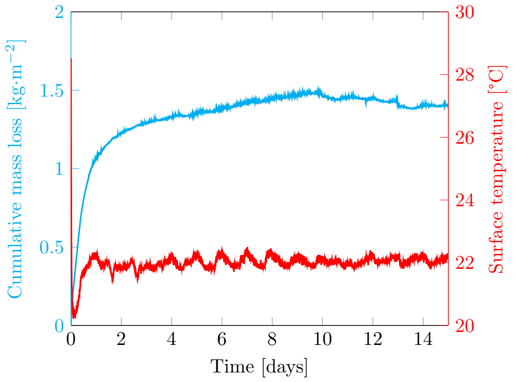

Figure 9: Mass and surface temperature evolution of cast mortar during 15 days at 22 °C and 50% RH.

Figure 10 shows good agreement between simulation results and experimental observations, both in surface temperature and mass loss. The decrease of surface temperature below room temperature is well captured due to heat exchange from water vaporisation. Three evaporation phases are well reproduced by the simulation: a first phase in the first hour where surface temperature is high and therefore evaporation rate is also elevated, then a second phase where the evaporation rate is nearly constant until approximately 10 hours, associated with a low surface temperature, and finally a last phase with a decreasing evaporation rate and a surface temperature which is in equilibrium with the ambient temperature.

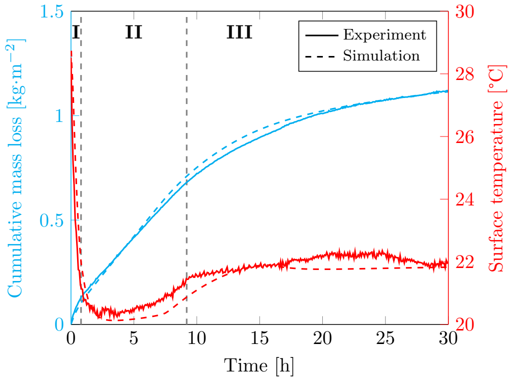

Figure 10: Comparison between simulated and observed evolutions of mass loss and surface temperature in the first 30 h.

6.3 Consequences on hardened properties

The loss of water due to evaporation impacts the hydration of the main binder greatly in the whole thickness of a layer. Figure 11 shows the simulated hydration profile of the main binder in a thin wall (30 mm) cured at different ambient relative humidities under 22 °C. Two phenomena are of interest here. Thirst, hydration in the entire thickness of the wall is affected by drying, with a significant reduction of the hydration degree at the center of the cross-section for all relative humidities of 80% and below. This decrease is comparatively more pronounced for higher relative humidities, while decrease in the hydration degree at the center of the cross-section is less significative when decreasing relative humidity below 70%. However, a second phenomenon is observed for lower relative humidities: the hydration profile is no longer homogeneous throughout the section; rather, there is a sharp decrease of hydration degree near the evaporation surface, creating a superficial layer of 3 to 4 mm where hydration is lower than in the bulk of the material.

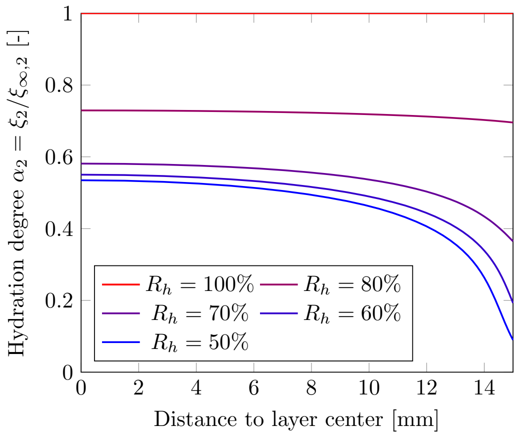

Figure 11: Main binder hydration degree profiles in the thickness of a 30 mm wide wall cured at different relative humidities.

This impact on hydration reflects directly in the strength of the material, leading to lower strength at lower ambient relative humidities, explaining the experimentally-observed loss of strength.

7 CONCLUSIONS AND PERSPECTIVES

A comprehensive modelling framework for 3D concrete printing, based on a multiphysics poromechanical model, has been used to investigate two crucial issues in 3D printing: the determination of adequate process parameters to ensure the printability of a given geometry, and the determination of the hardened properties of a print-piece given certain curing conditions. In both cases, the model was able to provide satisfying reproduction of experimental observations, allowing to explain the unerlying physical phenomena contributing to these observations. This paves the way for more complex simulations in 3D concrete printing, in order to predict and adapt the printing parameters and environment. In particular, drying shrinkage and cracking of print-pieces at the early age is a prime concern in 3D printing, due to the development of high capillary pressures with drying. Given an adequate failure criterion, the present model could be extended to the investigation of crack initiation in 3D print-pieces. The model's generality allows also for potential application in other fields of cement-based materials, such as shrinkage and cracking of cast concrete slabs, for instance.

REFERENCES

[1] Pierre, M., Samudio, M., Ghabezloo, S., and Dangla, P. 2025. Modelling the poromechanical behaviour of class G cement paste: a multiphysics approach from early age to hardened state. *Cement and Concrete Research* – In review.

[2] Wyrzykowski, M. and Lura, P. 2016. Effect of relative humidity decrease due to self-desiccation on the hydration kinetics of cement. *Cement and Concrete Research* **85**:75–81.

[3] Uno, P.J. 1998. Plastic shrinkage cracking and evaporation formulas. *ACI Materials Journal* **95**:365–375.

[4] Cervera, M., Oliver, J. and Prato, T. 1999. Thermo-Chemo-Mechanical Model for Concrete. I: Hydration and Aging. *Journal of Engineering Mechanics* **125**:1018–1027.

[5] Ma, L., Zhang, Q., Jia, Z., Liu, C., Deng, Z., and Zhang, Y. 2022. Effect of drying environment on mechanical properties, internal RH and pore structure of 3D printed concrete. *Construction and Building Materials* **315**:125731.

[6] Baratta, I.A., Dean, J.P., Dokken, J.S., Habera, M., Hale, J.S., Richardson, C.N., Rognes, M.E., Scroggs, M.W., Sime, N. and Wells, G.N. 2023. *DOLFINx: The next generation FEniCS problem solving environment.*

[7] Van Genuchten, M.T. 1980. A closed-form equation for predicting the hydraulic conductivity of unsaturated soils. *Soil science society of America journal* **44**(5):892–898.

[8] Mualem, Y. 1976. A new model for predicting the hydraulic conductivity of unsaturated porous media. *Water resources research* **12**(3):513–522.